Characterization of ultrafine coal fly ash particles by energy-filtered TEM

Y. CHEN, N. SHAH, F. E. HUGGINS, G. P. HUFFMAN & A. DOZIER
Consortium for Fossil Fuel Science / Department of Chemical and Materials Engineering, University of Kentucky, 533 South Limestone Street, Lexington, KY 40508-4005, U.S.A.

Summary

In this study, energy-filtered transmission electron microscopy is demonstrated to be a valuable tool for characterizing ultrafine coal fly ash particles, especially those particles encapsulated in or associated with carbon. By examining a series of elemental maps (K-edge maps of C and O, and L-edge maps of Si, Al, Ti and Fe) recorded using the three-window method, considerable numbers of titanium and iron species with sizes from several nanometres to submicrometre were shown to be present, typically as oxides dispersed in the carbonaceous matrix. Crystalline phases, such as rutile and iron-rich oxide spinel, were also identified from electron diffraction patterns and high-resolution TEM images. Information about these ultrafine coal fly ash particles regarding their size, morphology, elemental composition and distribution, and crystalline phases, which has not been available previously in conventional ash studies, should be useful in toxicological studies and related environmental fields.

Introduction

Coal combustion by electric utilities and power plants generates large quantities of fly ash that can have a significant impact on the environment. A 1000-MWe power station with a normal daily consumption of 12 000 tonnes of sub-bituminous coal produces about 2400 tonnes of fly ash a day. If a 99.95% capture efficiency rate is assumed for the electrostatic precipitators, about 1 tonne of fly ash per day is transferred to the environment by the power station (Querol *et al.*, 1996). Coal fly ash that is not trapped by pollution control devices contributes primarily to the fine particle component of particulate matter (PM) that is less than 2.5 μm in mean diameter ($PM_{2.5}$). Crocker *et al.* (2002) have established that coal fly ash can be a major component of ambient $PM_{2.5}$ in some locations. Compared with larger particles, $PM_{2.5}$ particles have longer residence times in the atmosphere and can be transported over greater distances. In addition, a given mass of smaller particles has more surface area than the same mass of larger particles, which makes them good carriers for some toxic volatile organic compounds (VOCs). Various studies have correlated the atmospheric concentration of ambient $PM_{2.5}$ particles with adverse health effects, such as an increased risk of pulmonary and cardiovascular diseases and mortality (Anderson *et al.*, 1992; Dockery & Pope, 1994). However, there are many uncertainties regarding the actual toxicological mechanisms, which are closely related with the physicochemical characteristics of individual $PM_{2.5}$ particles, such as size, morphology, crystallinity and chemical composition.

Analytical electron microscopy (AEM) is one of the most versatile tools for obtaining information about individual particles. The morphology, size and composition of micrometre and even submicrometre coal fly ash particles have been well characterized by a variety of electron microscopy techniques, including conventional scanning electron microscopy (SEM) (Quann & Sarofim, 1986; Seames, 2003), computer-controlled scanning electron microscopy (CCSEM) (Huffman *et al.*, 1989, 1990; Katrinak & Zygarlicke, 1995; O'Keefe *et al.*, 2000; Chen *et al.*, 2004), and conventional transmission electron microscopy (TEM) (Azar & Thomas, 1988; Qian *et al.*, 1988; Hurley & Schobert, 1992; Vassilev & Vassileva, 1996). However, scant information is available on ultrafine (< 100 nm) particles, which are abundant in coal fly ash $PM_{2.5}$ samples. Better information on the composition, structure and distribution of ultrafine particles is important for both adverse toxicological health effect studies and for understanding the mineral-to-ash transformation processes during combustion. Energy-filtered TEM (EFTEM) is a powerful tool that can be used to acquire elemental distribution maps with high lateral resolution and short acquisition times. Compared with traditional pixel-by-pixel scanning probe mapping in a TEM or SEM, which may take tens of minutes to hours to acquire a suitable elemental map, the acquisition time for an energy-filtered image acquired by

Correspondence to: Dr Naresh Shah. Fax: +1 859 257 7215; e-mail: naresh@uky.edu

EFTEM is typically seconds to tens of seconds. In addition, EFTEM can be used to obtain thickness maps that provide information about the third dimension of samples in addition to the two-dimension projections seen in bright-field images. EFTEM has been widely used in materials and biological sciences (Leapman & Hunt, 1995; Beckers *et al.*, 1996; Hofer *et al.*, 1996, 2000; Grogger *et al.*, 2000). However, applications of EFTEM in coal fly ash studies are limited. In a recent study, EFTEM was used to characterize uraninite aerosols collected near a coal power plant (Utsunomiya & Ewing, 2003). In this paper, we demonstrate that EFTEM, in combination with electron energy-loss spectroscopy (EELS), energy-dispersive X-ray spectroscopy (EDS), selected-area electron diffraction (SAED) and high-resolution TEM (HRTEM), can be used to investigate the elemental distribution, morphology, crystalline phase and electronic structure of individual coal fly ash particles, with emphasis on the ultrafine particles that may have the greatest impact on human health.

Materials and methods

Sample preparation

The combustion experiments were conducted at the U.S. Environmental Protection Agency (EPA) National Risk Management Research Laboratory (NRMRL) using a 50-kW, down-fired, refractory-lined pulverized-coal combustor (Linak *et al.*, 2000). Coal fly ash generated by combustion of high-volatile bituminous coal from western Kentucky was separated into fractions with mean aerodynamic diameter > 2.5 µm ($PM_{2.5+}$) and < 2.5 µm ($PM_{2.5}$) by means of a cyclone. Only the $PM_{2.5}$ fraction was examined in this study. Larger particles (> 0.3 µm) in both $PM_{2.5+}$ and $PM_{2.5}$ samples have been previously studied by CCSEM (Chen *et al.*, 2004). Samples for TEM observation were prepared by ultrasonicating a small amount of the $PM_{2.5}$ fly ash in acetone and then transferring several drops onto copper TEM grids coated with a lacey carbon film. Cross-section samples were also made by embedding $PM_{2.5}$ fly ash in EMBed-812 resin, then cutting ultrathin sections with a diamond knife in a Reichert Ultracut E ultramicrotome and depositing them on TEM copper grids coated with a lacey carbon film.

Instrumentation

The instrument used for this study was a 200-kV field emission analytical transmission electron microscope (JEOL JEM-2010F) equipped with an Oxford energy-dispersive X-ray spectrometer, a scanning (STEM) unit, and a Gatan imaging filter (GIF) system. The GIF system provides both energy-filtered imaging/diffraction and parallel-detection EELS. All images and spectra were recorded with a slow-scan charge coupled device (CCD) camera (1024 × 1024 pixel array) and processed with Gatan Digital Micrograph software. The energy-filtered images were recorded with a 150-µm condenser
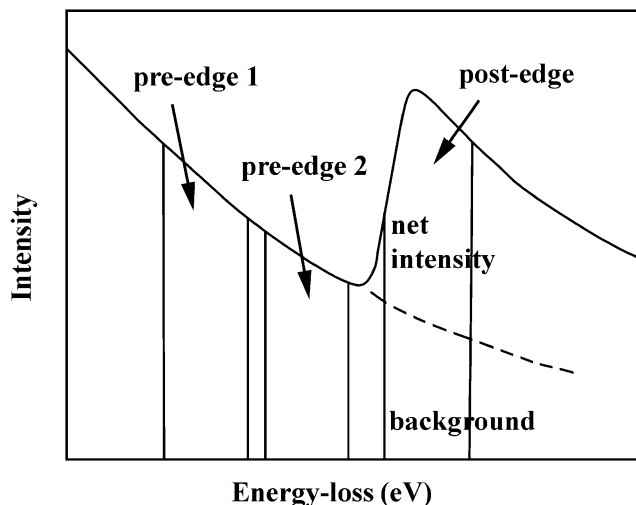

Fig. 1. Schematic diagram showing the three energy windows used for constructing an energy-filtered elemental map using the three-window method. The elemental map is obtained by subtracting the extrapolated background image calculated from the two pre-edge images from the post-edge image.

aperture and a 35-µm objective aperture. The three-window method (Jeanguillaume *et al.*, 1978; Egerton, 1996) was used to obtain the elemental maps. In this method, three images from the transmitted electrons filtered through three different energy regions with energy windows of predetermined width are collected sequentially using a CCD camera. As shown in Fig. 1, an extrapolated background image is calculated using the power-law model from the two pre-edge images, and then subtracted from the post-edge image, resulting in an elemental map with pixel intensity values that are proportional only to the actual concentration of the chosen element. The experimental parameters used for obtaining energy-filtered images of several selected elements in this study are listed in Table 1. Because an ionized element holds on to the remaining electrons more tightly, higher oxidation states of an element usually shift the onset of the ionization edge to higher energy. As a result, the ionization edges of an oxide can have a chemical shift of several electron volts compared with the pure element. The values of window positions in map settings are based on the real EELS spectrum of particles analysed in this study instead of the pure element values given in the literature. This is especially necessary when an unknown compound is being examined. To calibrate any edge position, the recording of the core-loss spectra of a particle was immediately preceded by recording of the zero-loss peak and the carbon K-edge spectrum of amorphous lacey carbon support film near the particle. The measured position of the carbon 1s-π^* peak was assigned a value of 285.4 eV to calibrate the energy. Linearity of the energy scale with this two-point calibration was calibrated during installation of the system. Frequent recalibration of energy is critical because the Gatan PEELS system can exhibit

Table 1. Experimental parameters for the acquisition of elemental maps using the three-window method.

	C-K	O-K	Al-L_3	Si-L_3	Ti-L_3	Fe-L_3
Elemental onset (eV)*	284.2	543.1	72.5	99.2	453.8	706.8
Experimental onset (eV)†	284	530	77	105	455	708
Pre-edge window 1(eV)	240–260	486–506	58–66	82–92	411–431	664–684
Pre-edge window 2 (eV)	260–280	506–526	66–74	92–102	431–451	684–704
Post-edge (eV)	285–305	531–551	78–86	106–116	456–476	709–729
Exposure time (s)	10	20	5	5	15	25

*Electron binding energy of pure element (from Thompson & Vaughan, 2001).

†Experimental edge value, which may have a chemical shift of several electron volts relative to that of pure element.

significant energy drifts due to even minute changes in the environment (e.g. movement of a chair in the room).

To provide complementary information to the elemental maps, EDS, EELS, SAED and HRTEM analyses were also conducted on selected representative particles. EDS spectra were recorded using an ultrathin-window detector and processed with the ES Vision program. EELS spectra were recorded in diffraction mode (image-coupled mode) using a beam convergence semi-angle of 1.4 mrad, a collection semi-angle of 4.2 mrad and a dispersion rate of 0.3 eV per channel. SAED and HRTEM were used to probe the microstructures of crystalline particles. The d-spacings from the diffraction patterns were compared with the International Center for Diffraction Data (ICDD) inorganic compound powder diffraction file (PDF) database and Inorganic Crystal Structure Database (ICSD) to identify the crystalline phases.

### Results and discussion

Titanium species

Our previous CCSEM studies on the western Kentucky coal fly ash showed that particles rich in silicon and aluminium (aluminosilicates) are dominant in the micrometre size range (> 0.5 μm) (Chen et al., 2004), whereas large numbers of titanium- and iron-containing particles are present in the ultrafine size range (Chen et al., 2005). Therefore, titanium and iron species are the main focus of this study.

Figure 2(a) shows the TEM bright-field image of a group of titanium-rich particles distributed in a char matrix. To differentiate the char matrix further from the titanium-rich particles, the carbon K-edge elemental map was recorded (Fig. 2b). The char matrix and lacey carbon edge appear bright in the carbon map, whereas inorganic particles and holes correspond to the dark regions. The titanium $L_{2,3}$-edge elemental map is shown in Fig. 2(c). In comparison with particles in the bright-field image, it is obvious that many of them are titanium-rich, stubby rods 50–100 nm in width and 100–300 nm in length. There are also some smaller (< 30 nm) titanium-rich particles that have weaker contrast but are still discernible in

the titanium map. Figure 2(d–f) shows the two background images taken before and a post-edge image taken after the titanium $L_{2,3}$-edge. Titanium-rich particles cannot be readily detected in the background images, but are clearly seen in Fig. 2(f), which is the image due to excitation of the titanium L ionization edge in the post-edge region. The differences between corresponding features in the post-edge and pre-edge background images provide a good indication of the presence of an element of interest.

Electron diffraction was conducted on some of the particles to verify whether these particles are crystalline or amorphous. The SAED pattern (Fig. 2g) recorded from the particle indicated by the arrow in the bright-field image was indexed as rutile (TiO_2) in the [111] zone axis. The titanium $L_{2,3}$-edge and oxygen K-edge EELS spectra recorded from this particle agree well with those of rutile. SAED patterns and EELS spectra recorded from a number of other particles (data not shown) confirm that these titanium-rich particles are basically rutile. As reported by Huggins et al. (1997) and Huggins & Huffman (2004), a large fraction of titanium in the western Kentucky no. 9 coal is associated with organic matrix in the form of organotitanium species. Consequently, the transformation of such organically bound titanium in the coal during combustion would likely result in the formation of nanocrystals of rutile (TiO_2).

Another Ti-rich species encountered in this study consists of titanium and aluminium-rich oxide particles. Figure 3(a) shows the TEM bright-field image of tens of titanium and aluminium-rich particles with sizes of less than 100 nm distributed in a char matrix. Due to interference from the char matrix, some of the smaller particles cannot be easily detected in the bright-field image. The titanium elemental map in Fig. 3(b) clearly reveals the titanium-rich particles that correspond to the bright regions in Fig. 3(a). However, smaller nanoparticles, down to a size of ~6 nm, are also detected in the titanium map. The aluminium $L_{2,3}$-edge elemental map is shown in Fig. 3(c). For most particles, the aluminium distribution correlates well with that of titanium, indicating that they are combined uniformly. Preliminary image analysis qualitatively indicates that the Ti/Al ratio is comparable across the
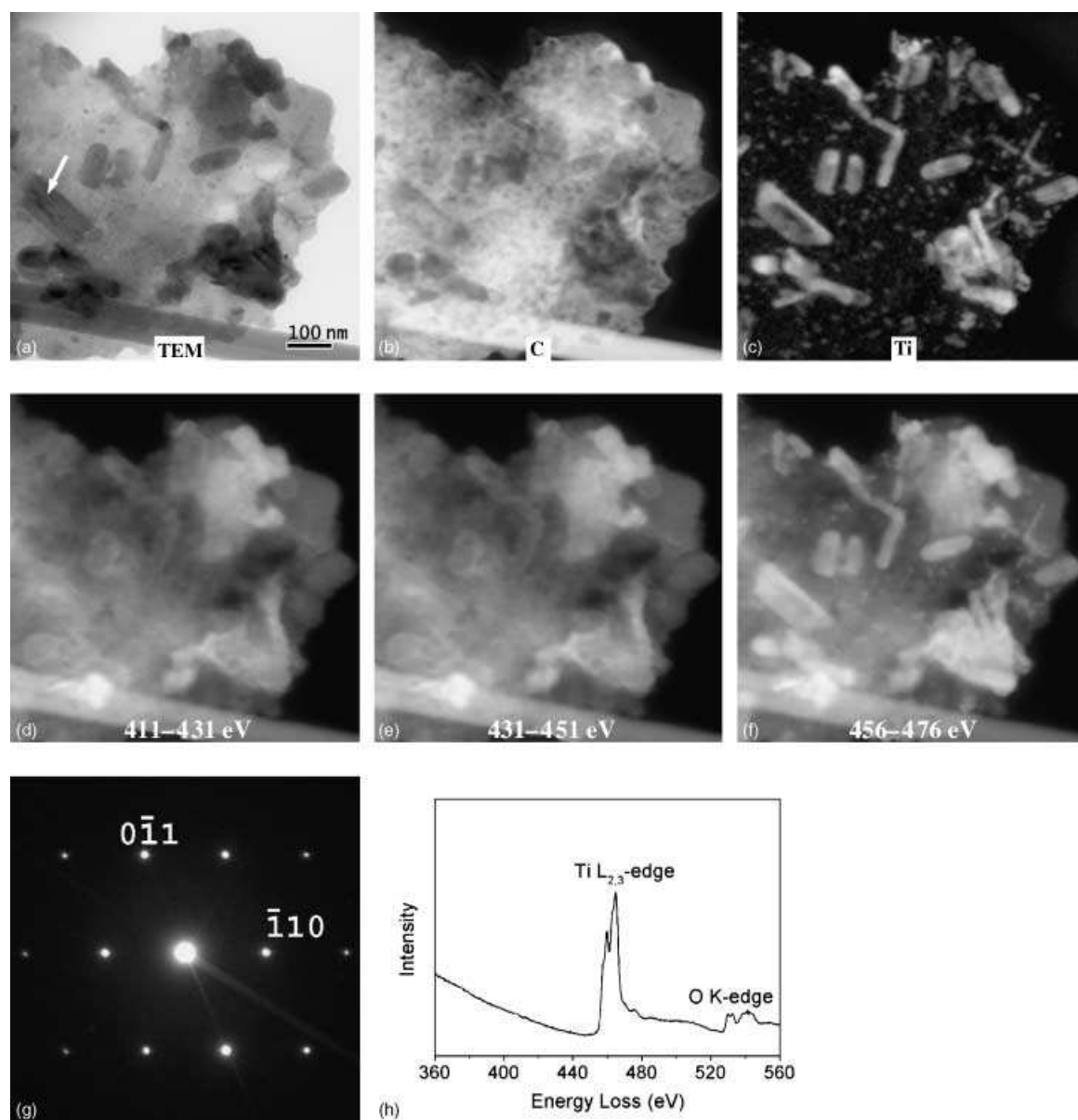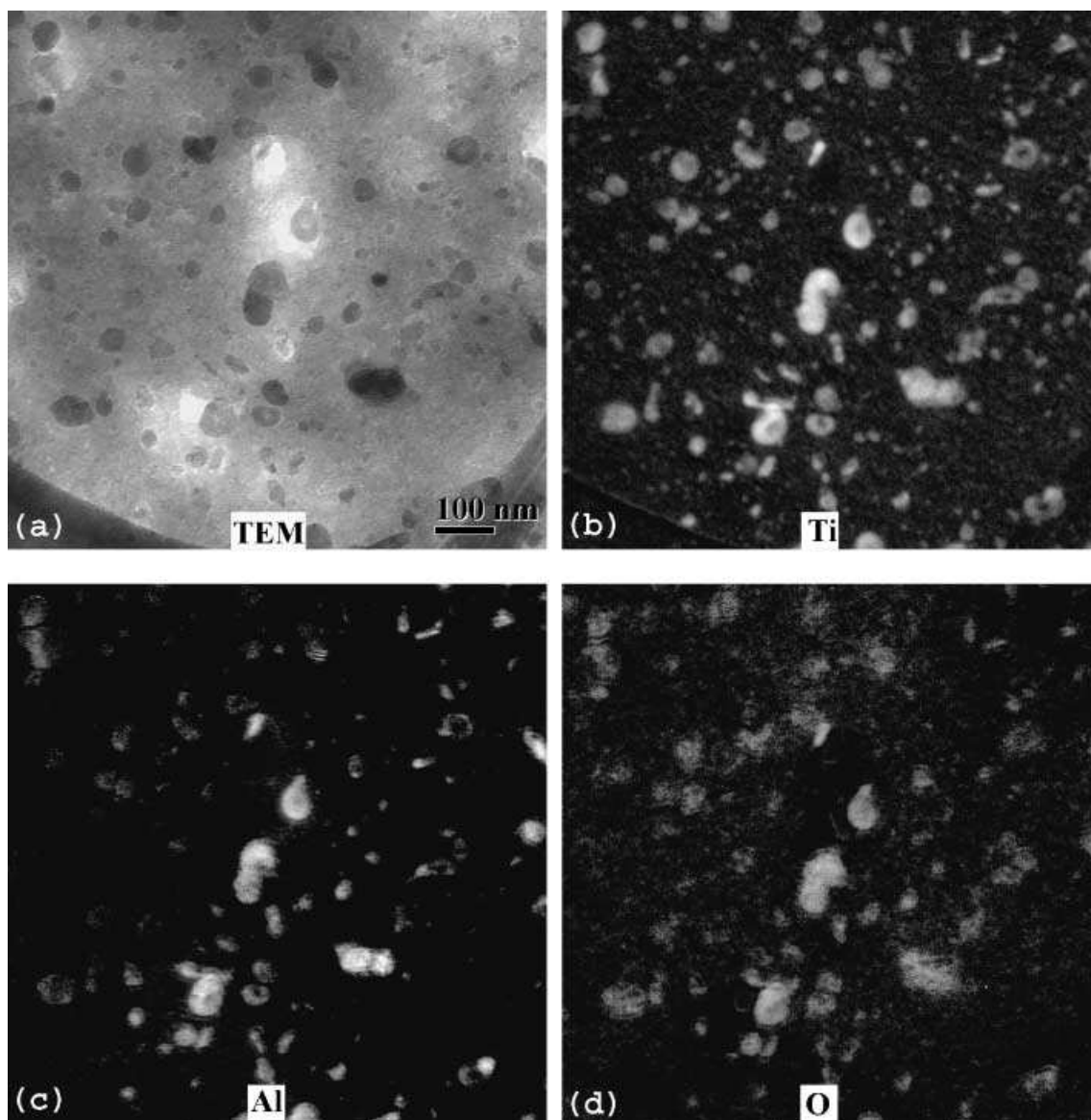
Fig. 2. Imaging of titanium-rich particles in a char matrix. (a) TEM bright-field image; (b) carbon K-edge elemental map; (c) titanium $L_{2,3}$-edge elemental map; (d–f) energy-filtered images corresponding to pre-edge 1 (411–431 eV), pre-edge 2 (431–451 eV) and post-edge (456–476 eV) regions of titanium $L_{2,3}$-edge map, respectively; (g) SAED pattern of the particle indicated by the arrow in (a) was indexed as rutile; (h) EELS spectrum of the particle indicated by the arrow in (a).

particles analysed. It should be noted that the carbon matrix and particle thickness can also affect the contrast in the maps. Because the plural scatterings from the carbon matrix decrease the signal-to-background ratio, small particles situated under a thick carbonaceous cover will show greater intensity diminution in the elemental maps. The bright regions in the oxygen elemental map (Fig. 3d) correlate with those in titanium and aluminium maps, indicating that these particles exist in the form of mixed titanium–aluminium oxides.

Iron species

Abundant iron-rich particles are also found in the fly ash sample and they typically exist either in iron-oxide form or in combination with other elements forming multi-element oxides. In high-sulphur western Kentucky coal, most of the iron is usually present in the form of pyrite (FeS_2) with marcasite as a minor component. During combustion, iron oxide particles would be expected to form from the decomposition, fragmentation and

Fig. 3. Imaging of titanium- and aluminium-rich nanoparticles in a char matrix. (a) TEM bright-field image; (b) titanium $L_{2,3}$-edge elemental map; (c) aluminium $L_{2,3}$-edge elemental map; (d) oxygen K-edge elemental map.

oxidation of these sulphide minerals (Huffman *et al.*, 1990). Figure 4(a) shows a TEM bright-field image of several iron-rich particles with angular shapes mixed in with carbonaceous matter. To differentiate iron-rich particles from the carbonaceous matter, carbon K-edge and iron $L_{2,3}$-edge elemental maps have been recorded and are shown in Fig. 4(b,c), respectively. In the carbon map, the carbonaceous matter is represented by the bright regions. The contours of iron-rich particles are also indicated from those dark regions. In the iron map, the iron-rich particles are revealed as bright regions, whereas the carbonaceous matter and carbon film support are dark. The SAED pattern (inset in Fig. 4c) recorded from the particles indicated by the arrow reveals a crystalline structure that

could be indexed as maghemite (γ-Fe$_2$O$_3$) in the [110] zone axis. The EELS spectra recorded from the same particles show oxygen K-edge and iron L_3-($2p_{3/2}$) and L_2-($2p_{1/2}$) edges, which confirm the iron-oxide nature of the particles. Further quantitative analysis of the ratio of iron to oxygen reveals a value of 0.65 ± 0.1 (close to $2:3$), indicating a trivalent iron oxide form.

Ultrafine iron-rich spherules were frequently observed in carbonaceous matrices. Figure 5(a) shows a TEM bright-field image of a carbonaceous matrix containing a group of iron-rich spherules. The success of observing these particles is closely related with the thickness of the carbonaceous matrix. Because most of these particles have a size less than 50 nm,
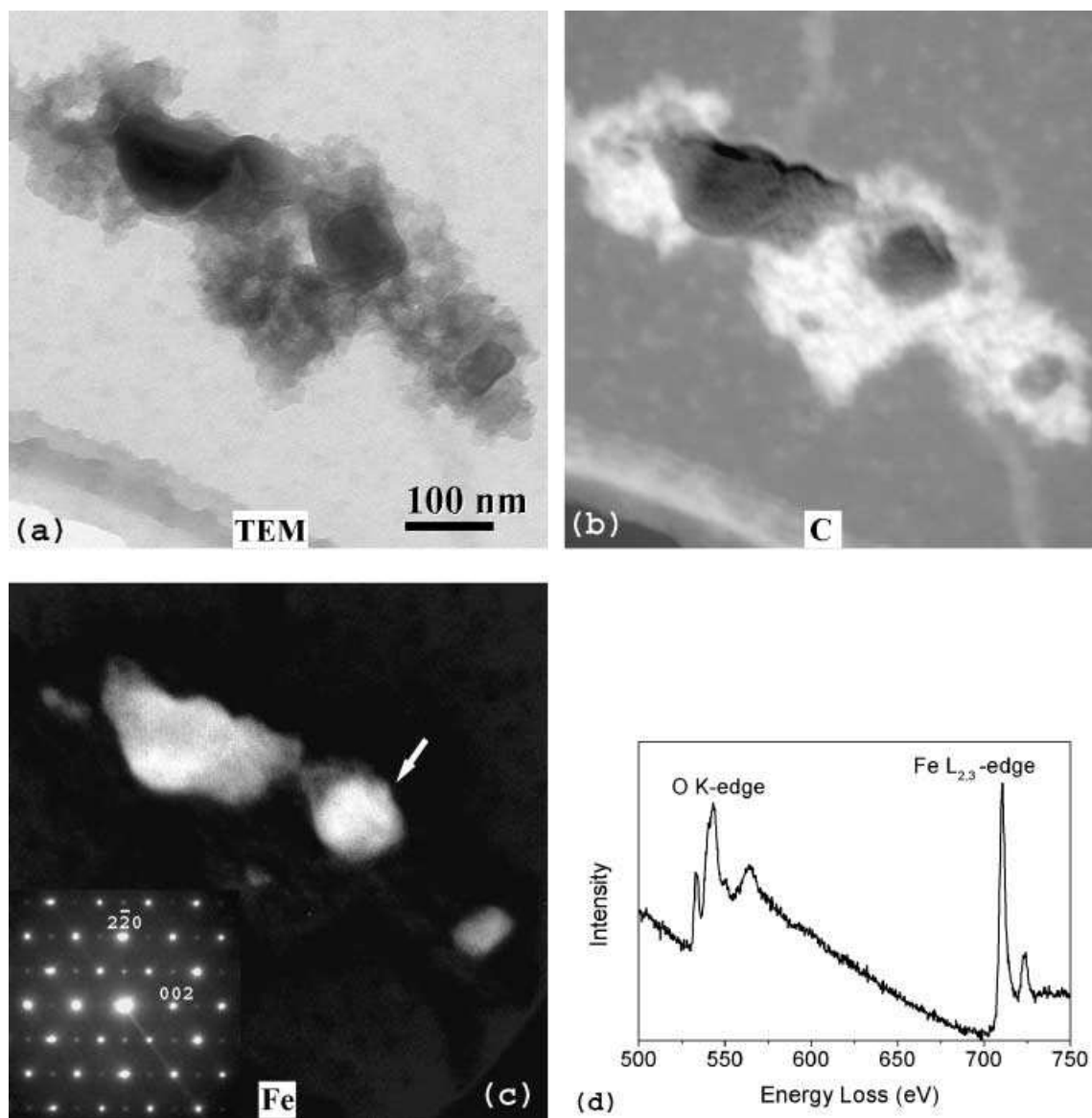
Fig. 4. (a) TEM bright-field image of iron-rich particles mixed with carbonaceous matter; (b) the carbonaceous matter is highlighted as bright regions in the carbon K-edge elemental map; (c) iron-rich particles are revealed in the iron $L_{2,3}$-edge elemental map, and the SAED pattern recorded from the particle indicated by the arrow is indexed as maghemite; (d) EELS spectrum recorded from the same particle indicated in (c) shows the near edge fine structure of the oxygen K-edge and iron $L_{2,3}$-edge.

a thick carbonaceous matrix may lead to a low signal-to-background ratio, hampering identification. As shown in the thickness map (Fig. 5b), the relative thickness, t/λ (t = thickness and λ = mean free path), from point A to point B shows a decreasing trend. For the portion with t/λ less than 1.5, which corresponds to the top right-hand section, the carbonaceous matrix is clearly revealed and has good contrast to the darker spherules in the carbon K-edge elemental map (Fig. 5c). The iron-rich particles are also clearly revealed in the iron $L_{2,3}$-edge elemental map (Fig. 5d). Much of the bright region in the iron map corresponds to the bright regions in the oxygen map, indicating an oxide form of these iron-rich particles. For the

portion of the A–B path with t/λ larger than 1.5, which corresponds to the bottom left-hand section, most features appear dark in the carbon map, even though it contains more carbonaceous matter. This is due to stronger inelastic scattering of the electrons in the thicker regions, which leads to lower contrast in the carbon elemental map. Therefore, even though iron signal is present in the EDS spectra recorded from this region, particle features are not detected in the iron map. The crystalline characteristic of the spherule indicated by the arrow in (a) was confirmed by its HRTEM image, shown in Fig. 5(f). Indexing of its fast Fourier transform (FFT) image further identifies the particle as magnetite.
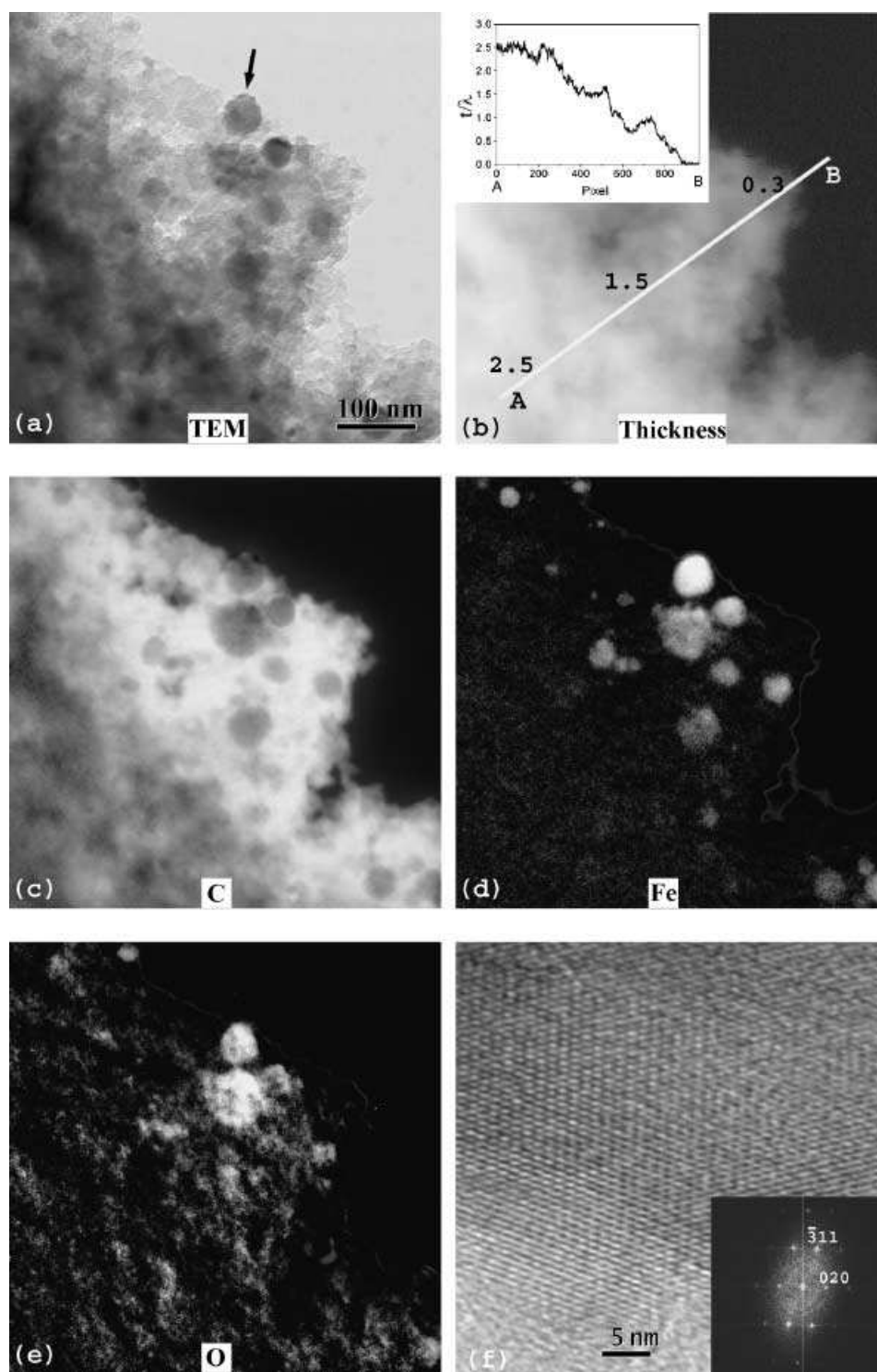
Fig. 5. Images of iron-rich spherules in a carbonaceous matrix of variable thickness. (a) TEM bright-field image; (b) thickness profile from A to B, showing decreasing relative thickness (t/λ); (c) carbon K-edge elemental map; (d) iron $L_{2,3}$-edge elemental map; (e) oxygen K-edge elemental map; (f) HRTEM image taken from the particle indicated by the arrow in (a) and the FFT of the image indexed as magnetite in the [103] zone axis (inset).
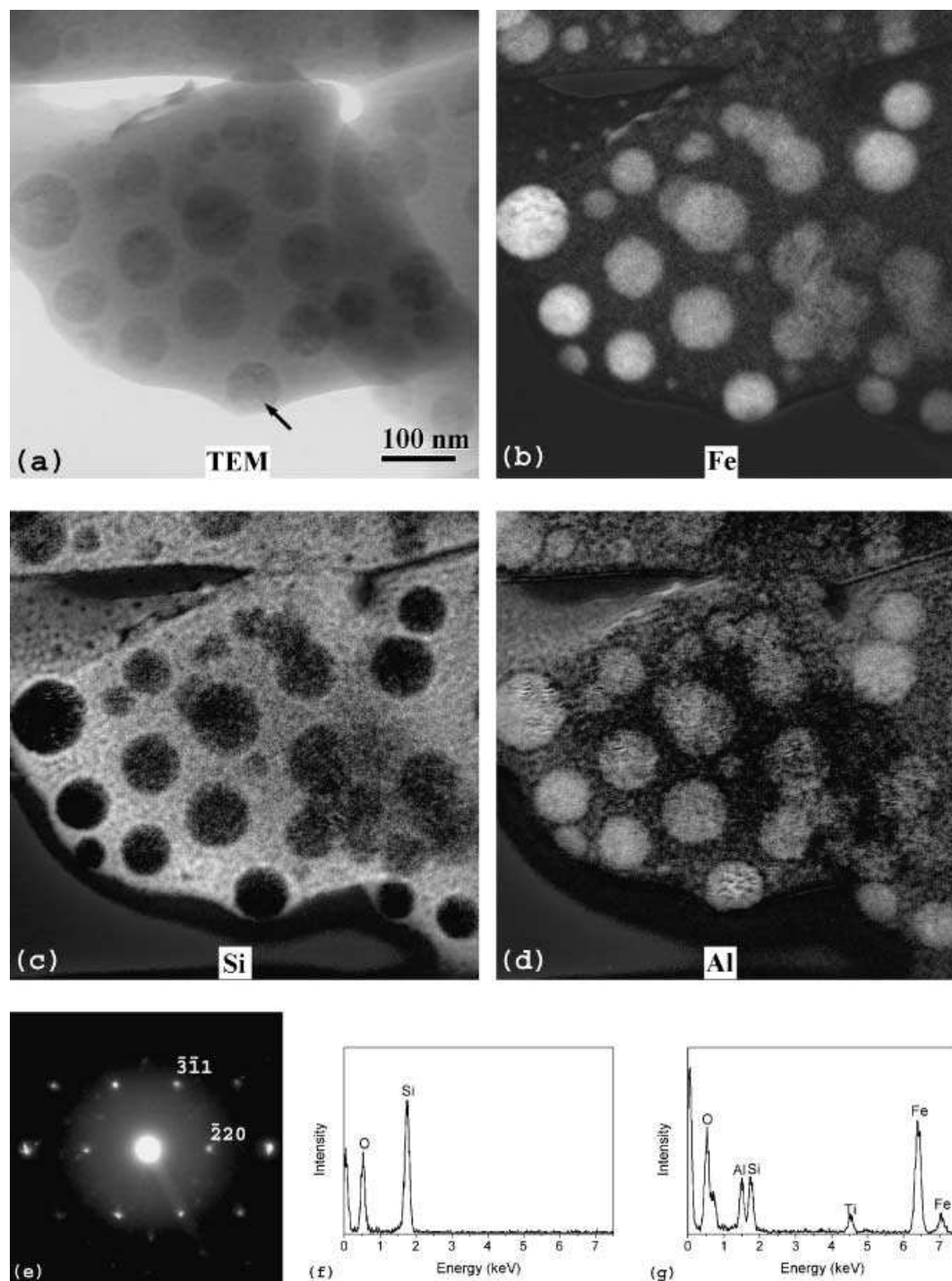
Fig. 6. A cluster of crystalline ultrafine iron and aluminium-rich spherules embedded in an amorphous silica matrix, forming a submicrometre Fe–Si–Al composite particle. (a) TEM bright-field image; (b) iron $L_{2,3}$-edge elemental map; (c) silicon $L_{2,3}$-edge elemental map; (d) aluminium $L_{2,3}$-edge elemental map; (e) SAED pattern recorded from the particle indicated by the arrow in (a) was indexed as Fe–Al oxide spinel; (f,g) EDS spectra recorded from the matrix and the spherule, respectively.

In CCSEM classification of eastern U.S. bituminous coal fly ash particles, Fe-aluminosilicate is often an important chemical category. Whether iron, aluminium and silicon are distributed uniformly in individual particles is an interesting question, which normally cannot be answered by SEM / EDS or CCSEM studies. EFTEM provides an answer to this question in a fast and convenient way. Figure 6(a) shows the TEM bright-field image of the cross-section of a submicrometre Fe-aluminosilicate

particle. The relative thickness t/λ of the cross-section is less than 1.1. A group of ultrafine spherules distributed in the matrix with lower contrast can be discerned. The $L_{2,3}$-edge elemental maps of iron, aluminium and silicon were recorded to provide more detailed elemental distribution information. The two pre-edge windows of the aluminium map were restricted to 63–75 eV in order to reduce possible interference from the iron $M_{2,3}$-edge (55 eV). In the iron map (Fig. 6b), the spherules show bright contrast, revealing iron-rich characteristics, whereas in the silicon map (Fig. 6c), they appear dark and the matrix shows bright contrast, clearly indicating a compositional difference between the spherules and the matrix. In the aluminium map (Fig. 6d), the aluminium is concentrated largely in the spherules and not in the matrix, indicating that the spherules also contain aluminium. EDS spectra recorded from the matrix and spherule are shown in Fig. 6(f,g), respectively. The silica-rich nature of the matrix is confirmed by the silicon and oxygen peaks appearing in the spectrum. The EDS spectrum recorded from the spherule shows mainly iron, aluminium and silicon. Because these spherules are embedded in a silica matrix, some contribution of the matrix to the spectrum is unavoidable. The SAED pattern (Fig. 6e) recorded from the particle indicated by the arrow in the bright-field image was indexed as a crystalline Fe–Al oxide with a cubic spinel-type structure. The amorphous nature of the silica matrix was confirmed by its SAED pattern, which showed diffuse diffraction rings. The above results clearly demonstrate that this Fe-aluminosilicate particle has a heterogeneous microstructure in which iron, aluminium and silicon are not uniformly distributed. Some other Fe-aluminosilicate particles consisting of iron-rich magnetite spherules in an aluminosilicate matrix were also observed in this study. These results indicate that iron, aluminium and silicon do not form a uniform oxide phase in these small Fe-aluminosilicate particles. We suspect that such structures most likely form as a result of the crystallization and precipitation of Fe–Al spinels in a molten iron aluminosilicate matrix.

Conclusions

EFTEM in combination with EELS, EDS, SAED and HRTEM has been employed to study coal fly ash particles generated from combustion of western Kentucky bituminous coal. Emphasis has been placed on the ultrafine particles that have a greater impact on human health and environmental issues. By examining a series of elemental maps, consisting of the K-edge maps of carbon and oxygen and the $L_{2,3}$-edge maps of titanium, iron, silicon and aluminium, abundant titanium- and iron-based nanoparticles were identified. Specific phases identified included titanium and iron oxides, and Ti–Al oxides, typically present as nanoparticles distributed in carbonaceous matrices. Heterogeneous elemental distributions of iron, aluminium and silicon in Fe-aluminosilicate particles were observed by examining ultrathin cross-sectioned samples. Such iron- and titanium-rich

particles exhibited highly crystalline characteristics, as evidenced from their SAED pattern or HRTEM images. This type of information regarding elemental spatial distributions and phase crystallinity in individual ultrafine and nanometre-sized particles has not been reported previously in conventional ash studies. Owing to the growing awareness of the importance of ultrafine particles in health issues from combustion-derived PM, we anticipate that such studies could be very significant for improved understanding of toxicological mechanisms in health effect studies involving coal fly ash and similar combustion-generated particles. EFTEM should therefore find wide application in environmental and combustion science studies.

References

Anderson, K.R., Avol, E.L., Edwards, S.A., Shamoo, D.A., Peng, R.C., Linn, W.S. & Hackney, J.D. (1992) Controlled exposures of volunteers to respirable carbon and sulphuric acid aerosols. *J. Air Waste Manage. Assoc.* **42**, 770–776.

Azar, H. & Thomas, S.J. (1988) Microcharacterization of micron/submicron fly ash from a pulverized-dry-coal-burning power plant. *Surface Interface Anal.* **13**, 142–148.

Beckers, A.L.D., Gelsema, E.S., De Bruijn, W.C., Cleton-Soeteman, M.I. & Van Eijk, H.G. (1996) Quantitative electron spectroscopic imaging in bio-medicine: evaluation and application. *J. Microsc.* **183**, 78–88.

Chen, Y., Shah, N., Huggins, F.E. & Huffman, G.P., (2005) Transmission electron microscopy investigation of ultrafine coal fly ash particles. *Environ. Sci. Technol.* **39**, in press.

Chen, Y., Shah, N., Huggins, F.E., Huffman, G.P., Linak, W.P. & Miller, C.A. (2004) Investigation of primary fine particulate matter from coal combustion by computer-controlled scanning electron microscopy. *Fuel Process. Technol.* **85**, 743–761.

Crocker, C.R., Eylands, K.E., McCollor, D.P., Helmowski, B.S., Benson, S.A. & Galbreath, K.C. (2002) Characterization of $PM_{2.5}$ from rural midwestern U.S. sites. *ACS, Fuel Chem. Division Preprints*, **47**, 632–633.

Dockery, D.W. & Pope, C.A. (1994) Acute respiratory effects of particulate air pollution. *Annu. Rev. Public Health*, **15**, 107–132.

Egerton, R.F. (1996) *Electron Energy Loss Spectroscopy in the Electron Microscope*, 2nd edn. Plenum Press, New York.

Grogger, W., Hofer, F., Warbichler, P. & Kothleitner, G. (2000) Quantitative energy-filtering transmission electron microscopy in materials science. *Microsc. Microanal.* **6**, 161–172.

Hofer, F., Grogger, W., Warbichler, P. & Papst, I. (2000) Quantitative energy-filtering transmission electron microscopy (EFTEM). *Mikrochim. Acta*, **132**, 273–288.

Hofer, F., Warbichler, P., Buchmayr, B. & Kleber, S. (1996) On the detection of MX-precipitates in microalloyed steels using energy-filtering TEM. *J. Microsc.* **184**, 163–174.

Huffman, G.P., Huggins, F.E., Levasseur, A.A., Chow, O., Srinivasachar, S. & Mehta, A.K. (1989) Investigation of the transformations of pyrite in a drop-tube furnace. *Fuel*, **68**, 485–490.

Huffman, G.P., Huggins, F.E. & Shah, N. (1990) Behavior of basic elements during coal combustion. *Prog. Energy Combustion Sci.* **16**, 293–302.

Huggins, F.E. & Huffman, G.P. (2004) How do lithophile elements occur in organic association in bituminous coals? *Int. J. Coal Geol.* **58**, 193–204.

Huggins, F.E., Srikantapura, S., Parekh, B.K., Blanchard, L. & Robertson, J.D. (1997) XANES spectroscopic characterization of selected elements in deep-cleaned fractions of Kentucky #9 coal. *Energy Fuels*, **11**, 691–701.

Hurley, J.P. & Schobert, H.H. (1992) Ash formation during pulverized subbituminous coal combustion. 1. Characterization of coals, and inorganic transformations during early stages of burnout. *Energy Fuels*, **6**, 47–58.

Jeanguillaume, C., Trebbia, P. & Colliex, C. (1978) About the use of electron energy-loss spectroscopy for chemical mapping of thin foils with high spatial resolution. *Ultramicroscopy*, **3**, 237–242.

Katrinak, K.A. & Zygarlicke, C.J. (1995) Size-related variations in coal fly ash composition as determined using automated scanning electron microscopy. *Fuel Process. Technol.* **44**, 71–79.

Leapman, R.D. & Hunt, J.A. (1995) Compositional imaging with electron energy loss spectroscopy. *J. Microsc. Soc. Am.* **1**, 93–108.

Linak, W.P., Miller, C.A. & Wendt, J.O.L. (2000) Comparison of particle size distributions and elemental partitioning from the combustion of pulverized coal and residual fuel oil. *J. Air Waste Manage. Assoc.* **50**, 1532–1544.

O'Keefe, C.A., Watne, T.M. & Hurley, J.P. (2000) Development of advanced scanning electron microscopy techniques for characterization of submicron ash. *Powder Technol.* **108**, 95–102.

Qian, J.C., Lachowski, E.E. & Glasser, F.P. (1988) The microstructure of National Bureau of Standards reference fly ashes. *Materials Res. Soc. Symp. Proceedings*, **136**, 77–85.

Quann, J.R. & Sarofim, A.F. (1986) A scanning electron microscopy study of the transformations of organically bound metals during lignite combustion. *Fuel*, **65**, 40–46.

Querol, X., Alastuey, A., Lopez-Soler, A., Mantilla, E. & Plana, F. (1996) Mineral composition of atmospheric particulates around a large coal-fired power station. *Atmos. Environ.* **30**, 3557–3572.

Seames, W.S. (2003) An initial study of the fine fragmentation fly ash particle mode generated during pulverized coal combustion. *Fuel Process. Technol.* **81**, 109–125.

Thompson, A.C. & Vaughan, D., eds (2001) *Center for X-Ray Optics and Advanced Light Source. X-Ray Data Booklet*, 2nd edn. Lawrence Berkley National Laboratory, California (also available at http://xdb.lbl.gov/).

Utsunomiya, S. & Ewing, R.C. (2003) Application of high-angle annular dark field scanning transmission electron microscopy, scanning transmission electron microscopy-energy dispersive X-ray spectrometry, and energy-filtered transmission electron microscopy to the characterization of nanoparticles in the environment. *Environ. Sci. Technol.* **37**, 786–791.

Vassilev, S.V. & Vassileva, C.G. (1996) Mineralogy of combustion wastes from coal-fired power stations. *Fuel Process. Technol.* **47**, 261–280.